Journal of Health Informatics

J Health Inform. 2026;18:e1817
DOI: https://doi.org/10.59681/2175-4411.v18.iEspecial.2026.1817

ARTIGO COMPLETO
CBIS 2026

TIME: a processor-in-the-loop validation for point-of-care electrical impedance tomography

TIME: validação processor-in-the-loop para tomografia por impedância elétrica no ponto de atendimento

Guilherme Corrêa Koller[1], José Jair Alves Mendes Junior[2], Fábio Pires Itturriet[3] ✉

ORCID: 0009-0009-8906-6383 · 0000-0001-5578-7734 · 0000-0003-3140-2259

[1] Departamento Acadêmico de Informática (DAINF), Universidade Tecnológica Federal do Paraná (UTFPR), Curitiba (PR), Brazil.

[2] Departamento Acadêmico de Eletrônica (DAELN) e Programa de Pós-Graduação em Engenharia Elétrica e Informática Industrial (CPGEI-CT), Universidade Tecnológica Federal do Paraná (UTFPR), Curitiba (PR), Brazil.

[3] Departamento Acadêmico de Eletrotécnica (DAELT) e Programa de Pós-Graduação em Engenharia Biomédica (PPGEB-CT), Universidade Tecnológica Federal do Paraná (UTFPR), Curitiba (PR), Brazil.

ARTICLE INFORMATION

TYPE
Artigo completo · CBIS 2026

IDENTIFIER
e1817

DOI
10.59681/2175-4411.v18.iEspecial.2026.1817

RECEIVED
17 May 2026

ACCEPTED
20 July 2026

REVIEW PROCESS
Double Blind Review

HANDLING EDITOR
Juliano de Souza Gaspar

ACCESS
Open, CC BY 4.0

CORRESPONDING AUTHOR
Fábio Pires Itturriet
fabioitturriet@utfpr.edu.br

LICENSE

This is an open access article published under the Creative Commons CC BY 4.0 license, which permits use, distribution, and reproduction in any medium, provided the original work is properly cited.

CC BY 4.0

ABSTRACT

Objective: This study aims to validate the implementation of the Linear Back-Projection (LBP) reconstruction algorithm on a 32-bit microcontroller for Point-of-Care (PoC) Electrical Impedance Tomography (EIT) systems. **Method:** A Processor-in-the-Loop (PiL) validation strategy was applied using the STM32F769I-DISCO (ARM Cortex-M7) platform, processing real experimental data from the FIPS database. **Results:** Results showed numerical equivalence compared to MATLAB for the LBP algorithm, achieving a processing rate of 2.3 frames per second, measured directly on the device interface. While showing correlations between 0.80 and 0.89 in low-complexity scenarios compared to the Gauss-Newton algorithm, the system displayed morphological limitations in highly heterogeneous cases. **Conclusion:** It is concluded that the solution is feasible for autonomous low-cost EIT devices, supporting decentralized screening within the Brazilian Digital Health context.

Keywords: Electric Impedance; Tomography; Point-of-Care Testing.

RESUMO

Objetivo: Este estudo visa validar a implementação do algoritmo de reconstrução Linear Back-Projection (LBP) em um microcontrolador de 32 bits para sistemas de Tomografia por Impedância Elétrica (EIT) no ponto de atendimento (Point-of-Care, PoC). **Método:** Foi aplicada uma estratégia de validação Processor-in-the-Loop (PiL) com a plataforma STM32F769I-DISCO (ARM Cortex-M7), processando dados experimentais reais da base FIPS. **Resultados:** Os resultados mostraram equivalência numérica em relação ao MATLAB para o algoritmo LBP, com taxa de processamento de 2,3 quadros por segundo, medida diretamente na interface do dispositivo. Embora tenha apresentado correlações entre 0,80 e 0,89 em cenários de baixa complexidade em comparação com o algoritmo de Gauss-Newton, o sistema exibiu limitações morfológicas em casos altamente heterogêneos. **Conclusão:** Conclui-se que a solução é viável para dispositivos de EIT autônomos e de baixo custo, apoiando a triagem descentralizada no contexto da Saúde Digital brasileira.

Descritores: Impedância Elétrica; Tomografia; Testes Imediatos.

CBIS 2026 XXI CONGRESSO BRASILEIRO DE INFORMÁTICA EM SAÚDE

Paper presented at the 21st Brazilian Congress of Health Informatics (CBIS 2026), held from September 23 to 25, 2026, in Brasília (DF), Brazil, and published in the CBIS 2026 section of the Journal of Health Informatics.

HOW TO CITE THIS ARTICLE: Koller GC, Mendes Junior JJA, Itturriet FP. TIME: a processor-in-the-loop validation for point-of-care electrical impedance tomography. J Health Inform 2026;18:e1817. doi: https://doi.org/10.59681/2175-4411.v18.iEspecial.2026.1817

1 INTRODUCTION

Real-time functional medical imaging remains challenging in Point-of-Care (PoC) scenarios, especially in contexts constrained by cost, infrastructure, and access to specialized equipment [1]. Traditional imaging techniques, such as mammography and magnetic resonance imaging, are well established in clinical practice [2]. However, they present limitations related to high cost, low portability, and, in some cases, exposure to ionizing radiation, limiting their use in hard-to-reach regions and in environments that require continuous bedside monitoring [3].

In this context, Electrical Impedance Tomography (EIT) has emerged as a functional imaging technique used for real-time lung monitoring, especially in intensive care units, enabling continuous assessment of ventilation without ionizing radiation [1]. It is a non-invasive, portable, low-cost technique based on injecting low-amplitude electrical currents (typically around 2 mA at 1 kHz) and measuring surface voltages. From these measurements, it is possible to reconstruct the electrical conductivity distribution of tissues [4]. Beyond pulmonary applications, EIT has also been investigated for the detection of oncological abnormalities, since malignant tissues exhibit dielectric properties distinct from healthy tissues, such as higher conductivity. Studies report sensitivities of approximately 75% and specificities of 82% for the detection of breast lesions, highlighting its potential as a screening tool [5]. However, EIT is limited by low spatial resolution and higher noise levels when compared to established imaging modalities like computed tomography or magnetic resonance imaging. As a result, EIT presents a trade-off: it provides less anatomical detail, but allows for continuous, real-time visualization directly at the bedside.

Recent literature presents different approaches to the portability of EIT systems. EIT-kit [6] proposes a set of tools that facilitates hardware design and provides a microcontroller library for calibration, but delegates image reconstruction to mobile devices via an API. Regarding embedded processing, San-Pablo-Juárez *et al.* [7] demonstrated the feasibility of solving the forward and inverse problems on 32-bit microcontrollers using the Sheffield back-projection algorithm, avoiding the need for external computers. On the other hand, the Flexi-EIT system [8] focuses on hardware flexibility with active electrodes and uses structured sparse optimization algorithms for reconstruction, but still relies on an external application for final image rendering. Despite these advances, most approaches still depend, fully or partially, on external processing for image reconstruction or visualization.

Furthermore, image reconstruction in EIT is an ill-posed and computationally intensive inverse problem, making its implementation on low-cost embedded systems difficult [9]. However, despite the recent advances in hardware flexibility and algorithmic design, the implementation and validation of fully autonomous EIT reconstruction pipelines on low-cost embedded platforms, using real experimental data and deterministic validation strategies such as Processor-in-the-Loop (PiL) [10], remain underexplored. Therefore, to address this scientific gap, this work proposes the implementation and validation of a Linear Back-Projection (LBP) algorithm on a 32-bit microcontroller. Validation is carried out through PiL testing, using real data from the Finnish Inverse Problems Society (FIPS) archive [11], and compared with reference methods such as the Gauss-Newton (GN) algorithm implemented in the EIDORS software [12].

The main contributions of this work are: (*i*) the implementation of a fully autonomous EIT system on a 32-bit microcontroller (ARM Cortex-M7), capable of performing image reconstruction and rendering locally, eliminating the dependence on external processing; (*ii*) the development of a validation architecture based on PiL, using physical data with instrumentation noise from the FIPS archive, providing a more realistic assessment of firmware performance; and (*iii*) the release of an open-source implementation, promoting reproducibility and extensibility of the proposed solution.

2 METHODS

The objective of this section is to describe the methodology used to evaluate the central research question: verify the accuracy and integrity of image reconstruction algorithms when subjected to the architectural limitations of a PoC device. To this end, a validation pipeline was structured, ranging from the ingestion of physical data to the extraction of comparative metrics. The architecture of this pipeline, which integrates data conversion, embedded processing, and host-side validation, is illustrated in Figure 1.

2.1 Database

Validation of the TIME platform was conducted using real experimental data from the Open 2D Electrical Impedance Tomography data archive [11], made available by FIPS. This dataset was chosen because it provides a clinically representative test, since the measurements were physically collected by the KIT4 tomograph. This ensures that the dataset contains intrinsic instrumentation noise and contact-impedance fluctuations, which are absent from synthetic data.

The experimental setup consisted of a cylindrical tank (28 cm diameter) with 16 rectangular electrodes, filled with saline solution (300 µS). The protocol applied 2 mA currents at 1 kHz across 79 injection patterns, yielding 1,264 voltage measurements

Figure 1. PiL validation pipeline from FIPS data ingestion.

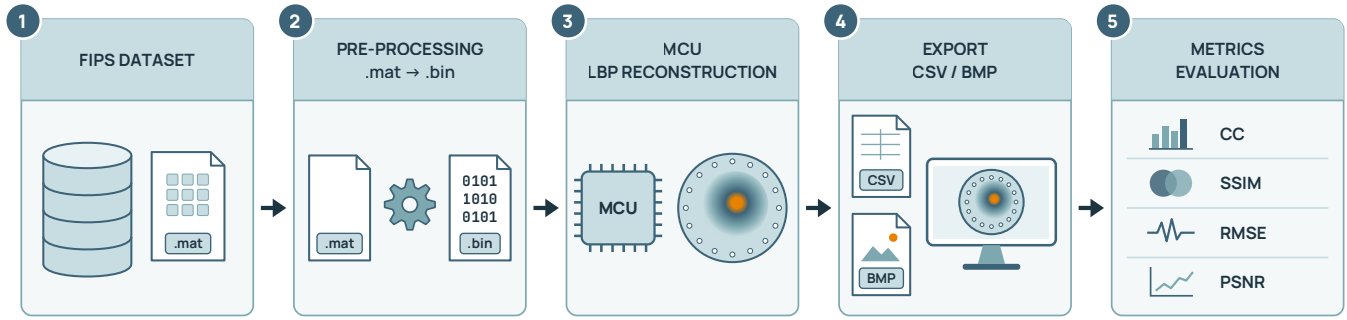

Source: Prepared by the authors (2026).

Figure 2. FIPS experimental setup. (a) Reference tank. (b) Tank with metallic and plastic inclusions. (c) Tank with organic material. (d) Tank with insulating foam and metallic inclusions.

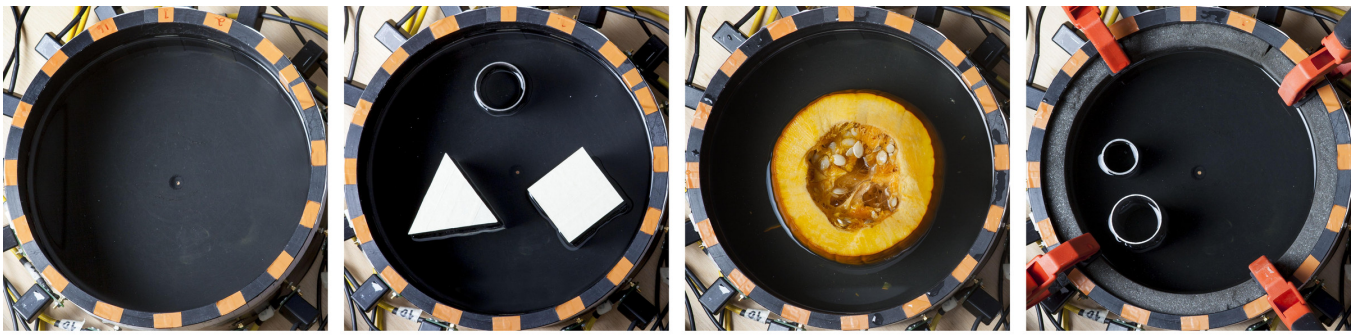

Source: Prepared by the authors (2026), adapted from [11].

per frame. The archive comprises 38 datasets: one homogeneous reference case and 37 datasets containing different anomalies (resistive plastic inclusions and conductive metallic inclusions) [11]. The FIPS dataset provides three main matrices per frame. The measured voltage matrix (Uel) has dimensions 16 × 79, where each row corresponds to a measurement pair and each column represents an injection pattern. The current injection pattern (CurrentPattern), also sized 16 × 79, defines the electrodes responsible for current injection using +1 and −1 values for each pattern. Additionally, the voltage measurement pattern (MeasPattern) is represented by a 16 × 16 matrix, where each row specifies the electrode pairs used for voltage acquisition. Figure 2 illustrates the experimental tank configuration, highlighting the reference tank and the phantom tank.

The 37 anomaly datasets are organized into eight groups (D1-D8) and divided into two evaluation scenarios with increasing reconstruction complexity. Scenario 1 (Groups D1-D5, 22 datasets) contains localized discrete inclusions with small to medium conductivity perturbations, remaining largely compatible with the linear assumptions of the LBP method. Scenario 2 (Groups D6-D8, 15 datasets) introduces spatially distributed, high-heterogeneity perturbations that substantially violate the small-perturbation assumption and represent the most challenging conditions for linear reconstruction.

Scenario 1 contains discrete inclusions (D1-D5): Groups D1-D5 consist of localized resistive plastic and/or conductive metallic inclusions with progressively increasing spatial complexity. Group D1 (4 datasets) contains a single small resistive plastic cylinder positioned at different locations in the domain, representing the simplest perturbation case and serving as a baseline for isolated anomalies. Group D2 (6 datasets) introduces two simultaneous resistive inclusions, a triangular object and a circular disk, arranged in different positional configurations. Group D3 (6 datasets) further increases complexity by combining three simultaneous inclusions, either resistive plastic objects (circular, square, and triangular shapes) or conductive metallic hollow cylinders, with varying positions and orientations, resulting in denser anomaly distributions. Group D4 (4 datasets) combines inclusions with opposite conductivity contrasts: a conductive metallic hollow cylinder filled with saline and a resistive plastic inclusion (triangular in datasets 4_1 and 4_2, and circular in datasets 4_3 and 4_4), producing competing conductive and resistive responses. Finally, Group D5 (2 datasets) contains three simultaneous mixed inclusions: a conductive metallic ring together with a plastic triangle and square (dataset 5_1), or two conductive metallic rings

Figure 3. Embedded implementation on STM32F769I-DISCO. (a) TIME starting interface. (b) Real-time image reconstruction using the LBP algorithm on the MCU.

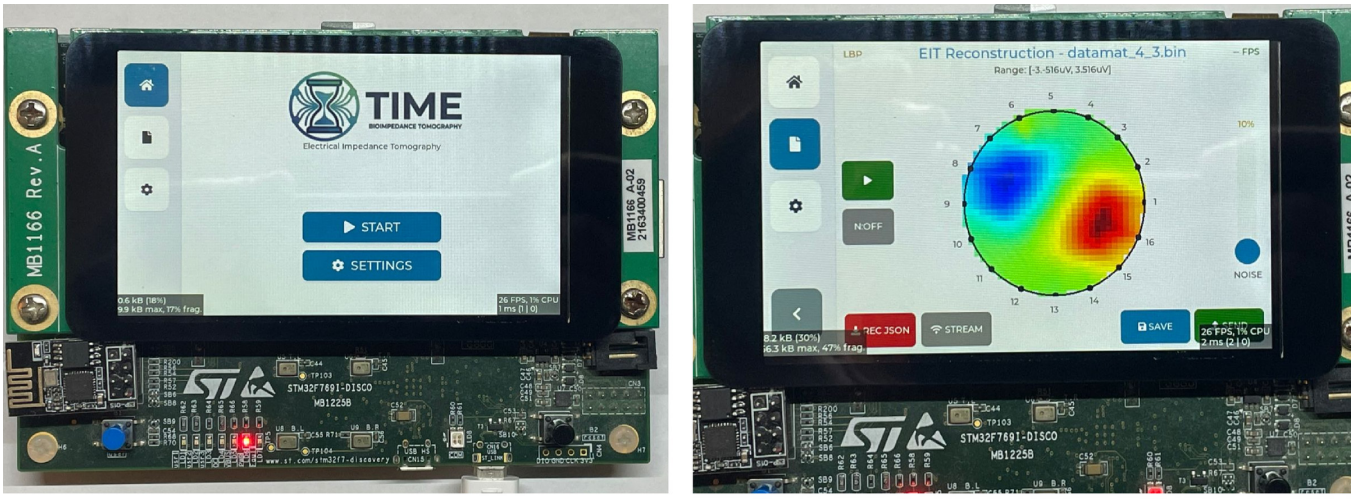

a) b)

Source: Prepared by the authors (2026).

together with a plastic triangle (dataset 5_2), representing the most complex discrete-inclusion configuration within Scenario 1.

Scenario 2 contains distributed perturbations (D6-D8): Groups D6-D8 contain large-scale, spatially distributed perturbations that globally alter the domain's conductivity field. Group D6 (7 datasets) consists of a gray insulating foam ring (~2 cm thick) positioned along the internal perimeter of the tank and in direct contact with all 16 electrodes. Depending on the dataset, discrete metallic or plastic inclusions are additionally placed inside the ring. In all cases, the ring modifies the boundary conditions across the entire domain, generating a strong distributed peripheral perturbation. Group D7 (2 datasets) contains a large organic inclusion formed by a half pumpkin submerged in saline. Due to its conductive pulp and heterogeneous internal composition (pulp, seeds, and fibers), the object occupies a substantial portion of the imaging domain and produces highly non-uniform conductivity distributions. Group D8 (6 datasets) combines the insulating foam ring with saline contaminated by organic residues from the pumpkin experiments, resulting in turbid saline containing suspended particles and spatial conductivity fluctuations. This group represents the highest heterogeneity level in the entire dataset and the most adverse reconstruction condition evaluated in this study.

2.2 Pre-processing

The processing flow required adapting the raw data to the microcontroller's architectural limits. This involved converting the original .mat files (in double precision) on the host into binary (.bin) files. At this stage, we converted the absolute voltage readings to float32 and compacted the electrode masks to int8 to optimize storage and data transfer.

The binary (.bin) file was structured to allow efficient sequential reading on the microcontroller. The file begins with a header containing a magic number (uint32) for validation, followed by metadata fields including the number of measurements, number of injections, and image size (all stored as uint8). The data section then stores the voltage matrix (Uel) in float32 format, followed by the current injection pattern (CurrentPattern) and the measurement pattern (MeasPattern), both stored as int8 arrays.

2.3 Embedded Implementation

Edge processing was carried out using the STM32F769I-DISCO development board (ARM Cortex-M7) [13]. The choice of this platform, shown in Figure 3, was based on its ability to store the sensitivity matrix entirely in its 16 MB external SDRAM and on the FPU's native acceleration for single-precision operations.

Image reconstruction was performed using the LBP algorithm [4], selected due to its low computational complexity and suitability for real-time embedded execution. The method operates on two voltage measurement vectors: a reference measurement acquired in a homogeneous medium and a target measurement containing conductivity perturbations. The reconstruction process is based on the differential voltage vector:

$$\Delta v = U_{target} - U_{ref} \quad (1)$$

where U_{target} denotes the voltage measurement vector acquired from the tank containing the anomaly and U_{ref} corresponds to the homogeneous saline reference

measurement. Both vectors contain M = 1264 voltage measurements. The resulting differential vector $\Delta v \in \mathbb{R}^M$ isolates conductivity perturbations relative to the baseline condition.

The reconstructed image, corresponding to the spatial distribution of conductivity variations ($\hat{x}$), is obtained by applying a linear transformation based on the sensitivity matrix:

$$\hat{x} = S^T \cdot \Delta v \quad (2)$$

where $\hat{x} \in \mathbb{R}^N$ represents the reconstructed image containing the spatial distribution of conductivity variations over the N = 1024 pixels of the 32×32 reconstruction grid. The sensitivity matrix $S \in \mathbb{R}^{M \times N}$ models the relationship between conductivity changes and voltage variations at the electrodes. Its construction uses a two-dimensional analytical electric field model: for each electrode positioned at (x_e, y_e) on the periphery of the unit circular domain, the electric field at pixel p located at (x_p, y_p) is:

$$\vec{E_e}(p) = \frac{1}{r^2}\begin{pmatrix} x_p - x_e \\ y_p - y_e \end{pmatrix} \quad (3)$$

The reconstruction grid is a 32 × 32 square (1024 pixels) grid in the interval [−1, 1; +1, 1] in normalized coordinates, with a circular mask of radius R ≤ 1 restricting reconstruction to the interior of the domain (~804 valid pixels). The sensitivity at pixel p for the pair (injection i, measurement m) is:

$$S_{(i \cdot n_{meas} + m),\, p} = \vec{E}^{(i)}_{inj}(p) \cdot \vec{E}^{(m)}_{meas}(p) \quad (4)$$

where $\boldsymbol{E}_{inj}{}^{(i)}(p)$ and $\boldsymbol{E}_{meas}{}^{(m)}(p)$ correspond to the electric field contributions generated by the current injection pair i and the voltage measurement pair m, respectively. Their dot product defines the sensitivity contribution at pixel p, populating the corresponding row of the sensitivity matrix.

The reconstruction stage involves more than one million multiply-accumulate operations per frame, representing the primary computational bottleneck of the system. To ensure deterministic real-time execution without cache exhaustion, all matrices were statically allocated in external SDRAM memory. During initialization, the sensitivity matrix is loaded into SDRAM, enabling direct memory access and allowing image reconstruction and rendering to be completed within milliseconds.

2.4 Validation Strategy

To evaluate numerical precision in an unbiased manner, the PiL validation methodology [10] was adopted, as it allows deterministic control of the input variables. This conceptual model ensures deterministic replay of the FIPS datasets. The replay component replaces the analog acquisition module with a simulated backend executed natively on the MCU. Acquisition is governed by a sequential state machine that simulates the transitions of an EIT analog front-end, with the states (*i*) idle, (*ii*) injection, and (*iii*) measuring. Timing simulation is essential to model the temporal latency of a real EIT analog front-end. Each of the 79 injection patterns follows a cycle with two configurable intervals:

- Current injection: models the current-source settling time.
- Voltage measurement: represents the ADC conversion times at the electrodes.

Using a default value of 1 ms per stage, the total acquisition time is 158 ms per frame, providing a realistic timing model for deterministic processing. This timing, combined with LBP reconstruction and graphical rendering, yields a real-time output of 2.3 frames per second, an empirical measurement visualized directly on the device interface. After inference, the reconstructed image matrix is exported to the SD card in CSV format (32 × 32, scientific notation, NaN outside the circular mask) and imported into MATLAB for comparison with reference implementations.

2.5 Evaluation Metrics

System accuracy was evaluated by comparing the MCU implementation (float32), MATLAB (reference LBP in double precision), and the nonlinear GN reconstruction from the EIDORS framework [12]. Performance was assessed using complementary image metrics: Pearson Correlation Coefficient (CC) and Structural Similarity Index (SSIM) for structural similarity, Root Mean Squared Error (RMSE) and Global Relative Error (GRE) for magnitude error, and Peak Signal-to-Noise Ratio (PSNR) for perceptual quality.

3 RESULTS

Thirty-seven datasets from the FIPS archive were processed, generating reconstructed images for each frame. The analysis evaluates the numerical equivalence between the TIME prototype and a reference MATLAB implementation, and the comparison between LBP and GN reconstructions.

3.1 Groups D1-D5

Groups D1-D5 include small resistive and conductive inclusions. In this group, the embedded LBP achieved CC values from 0.80 to 0.89 and SSIM between 0.47 and 0.90. Figures 4 and 5 show representative examples (Datasets 3_4 and 5_2), illustrating consistent spatial localization of the inclusions.

Figure 4. Dataset 3_4. (a) Phantom configuration. (b) EIDORS reconstruction using GN. (c) MCU reconstruction using LBP. (d) MATLAB reconstruction using LBP.

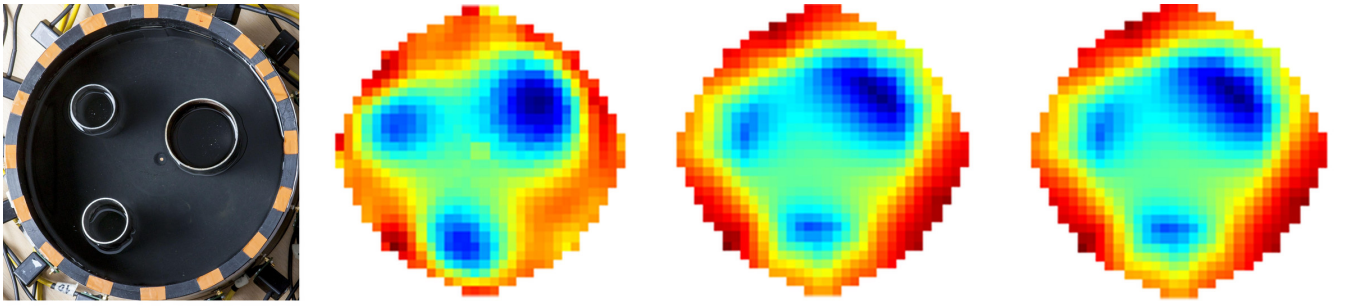

Source: Prepared by the authors (2026).

Figure 5. Additional low-complexity example: Dataset 5_2. (a) Phantom configuration. (b) EIDORS reconstruction using GN. (c) MCU reconstruction using LBP. (d) MATLAB reconstruction using LBP.

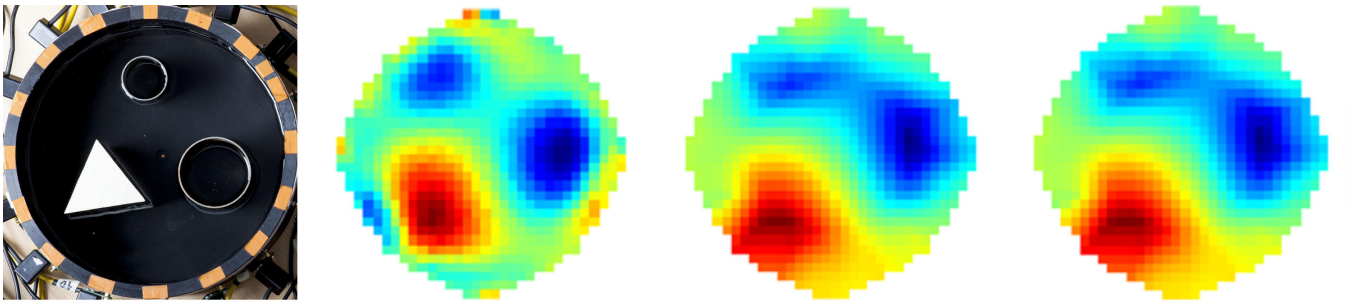

Source: Prepared by the authors (2026).

Figure 6. High-complexity scenarios (dataset 7_1). (a) Phantom configuration. (b) EIDORS reconstruction using GN. (c) MCU reconstruction using LBP. (d) MATLAB reconstruction using LBP. LBP results show shape distortion compared to GN.

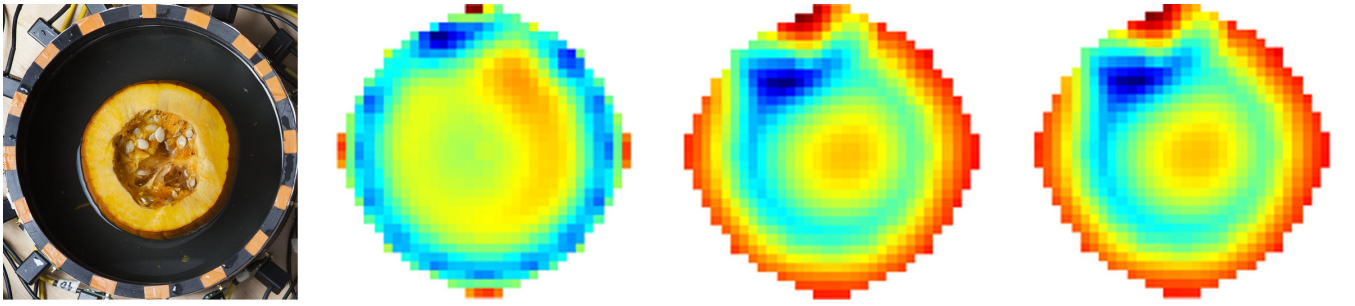

Source: Prepared by the authors (2026).

Figure 7. Reconstruction of dataset 6_3. (a) Phantom configuration. (b) EIDORS reconstruction. (c) MCU reconstruction. (d) MATLAB reconstruction.

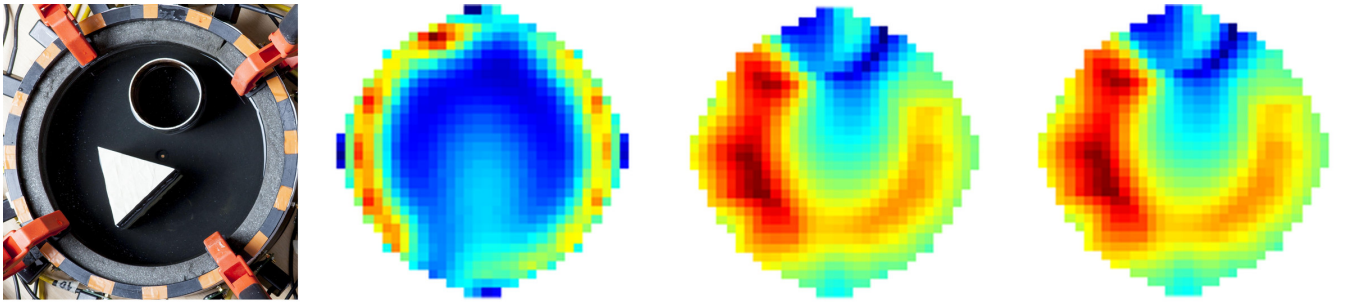

Source: Prepared by the authors (2026).

Table 1. Validation statistics calculated over 37 target datasets.

Metric	TIME vs. MATLAB (LBP) Average (SD)	TIME vs. EIDORS (GN) Average (SD)
CC	1.00 (0.00)	0.43 (0.52)
SSIM	1.00 (0.00)	0.59 (0.28)
GRE	0.00 (0.00)	1.52 (0.52)
RMSE	0.00 (0.00)	0.19 (0.07)
PSNR (dB)	128.80 (3.49)	14.97 (3.04)

Source: Prepared by the authors (2026).

Figure 8. Quantitative comparison by scenario and dataset group (D) complexity. (a) Pearson Correlation Coefficient (CC). (b) Structural Similarity Index (SSIM). Agreement is higher in low-complexity scenarios, with degradation in more complex cases.

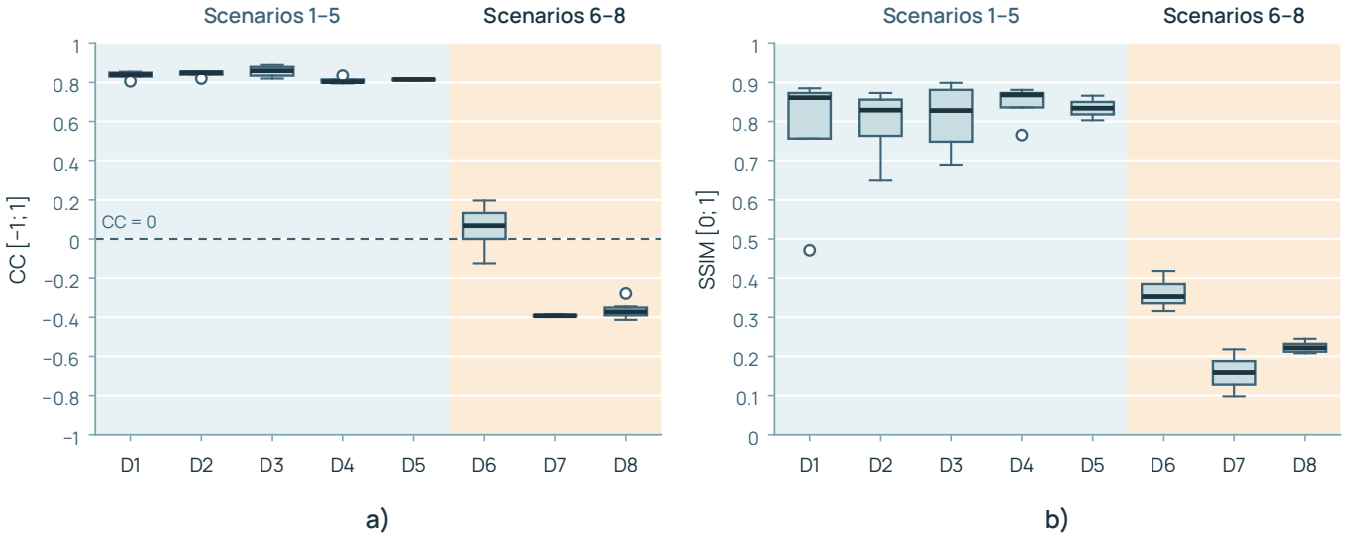

Source: Prepared by the authors (2026).

3.2 Groups D6-D8

Groups D6-D8 include larger, irregular, or high-conductivity inclusions. In this group, agreement between LBP and GN decreases, with CC values ranging from -0.41 to 0.20 and SSIM from 0.10 to 0.42. Figures 6 and 7 illustrate representative cases. In all datasets, the TIME vs. MATLAB comparison maintained CC = 1.00.

3.3 Quantitative Evaluation

Following the visual analysis, the numerical equivalence and accuracy of the TIME prototype were quantified. Table 1 presents the global descriptive statistics calculated over all 37 datasets.

The comparison between TIME and MATLAB revealed numerical equivalence across all 37 datasets, with CC and SSIM values of 1.00 (Table 1). In parallel, the RMSE and the GRE recorded values on the order of $\approx 10^{-7}$. The PSNR achieved a mean of 128.80 dB, with a minimum value of 120.92 dB.

While the global average in Table 1 indicates moderate agreement with EIDORS (Mean CC = 0.43), this aggregate value is heavily skewed downward by LBP's structural limitations in high-complexity scenarios. To better illustrate this variance and explain the results, we segmented the performance metrics (CC and SSIM) by image group, as shown in the boxplots in Figure 8.

The results show strong correlation and structural similarity for localized anomalies (Groups D1-D5). In contrast, Groups D6-D8 exhibit greater dispersion and reduced metric values, indicating reduced morphological fidelity in more complex targets. Two notable outliers are observed: datamat_1_1 (D1, SSIM = 0.47), where an inclusion at intermediate radial depth produces broader unregularized LBP spreading due to overlapping sensitivity contributions from all electrode pairs, and datamat_4_2 (D4, SSIM = 0.77), where opposite-polarity inclusions, a conductive metallic hollow cylinder and a resistive plastic triangle, are reconstructed differently by the two algorithms: the regularized GN solution distributes both contrast polarities in a balanced spatial pattern, while the unregularized LBP concentrates predominantly the positive conductive response, reducing structural agreement.

4 DISCUSSION

The numerical equivalence observed in the TIME vs. MATLAB/LBP comparison across all 37 datasets confirms that the LBP implementation in the firmware

is arithmetically correct: the residual discrepancies arise exclusively from precision differences between float32 on the MCU and double in MATLAB, with no logic or ordering error.

The comparison with the EIDORS/GN baseline revealed two distinct behaviors consistent with known LBP limitations. In low-complexity scenarios (Groups D1-D5, CC = 0.80-0.89), the results are consistent with previous reports [4] for linear back-projection methods: LBP provides acceptable topological localization of anomalies as long as the conductivity variation is moderate and the signal-to-noise ratio of the measurements is favorable [4]. Degradation in Groups D6-D8 (CC to -0.41) aligns with Lionheart's observations: single-step methods without regularization amplify errors when conductivity distributions violate small-perturbation assumptions, a condition frequently not satisfied by large-area conductive inclusions in highly heterogeneous scenarios [9]. The TIME vs. MATLAB comparison remains CC = 1.00 in all these cases, confirming that the divergence stems from the difference in mathematical formulation between linear LBP and iterative GN, not from defects in the embedded implementation.

Lionheart also notes that iterative algorithms with regularization tend to outperform linear methods in morphological fidelity for anomalies with complex geometry, at the cost of orders of magnitude more processing time [9]. This trade-off is central to the PoC context: the TIME platform sacrifices morphological fidelity in complex scenarios in favor of real-time execution on low-cost hardware.

5 CONCLUSIONS

The development and validation of the TIME prototype demonstrate the technical feasibility and computational efficiency of embedded Electrical Impedance Tomography for PoC screening applications. The PiL methodology based on FIPS experimental data confirmed that the LBP implementation on the microcontroller is arithmetically correct, achieving numerical equivalence with the reference workstation across all evaluated datasets. However, the comparative evaluation with the GN algorithm is purely contextual, as they possess different mathematical formulations and GN is not treated as a ground truth. The lower agreement and morphological distortions observed in Groups D6-D8 highlight known limitations of the LBP method rather than firmware errors or diagnostic failures of the TIME platform. This limitation is especially relevant for future oncological screening applications, which require greater morphological fidelity than LBP can provide on its own.

In the PoC context, the TIME platform shows that it is not necessary to concentrate all computational power in the edge device. Integration with Internet of Medical Things (IoMT) architectures represents a path to overcome this limitation: the MCU executes LBP in real time for immediate screening, while selected frames are transmitted via Wi-Fi to a remote server responsible for high-fidelity iterative reconstruction (Gauss-Newton or machine-learning-based algorithms). This edge-cloud architecture maintains real-time responsiveness without sacrificing diagnostic quality in complex cases.

The TIME prototype supports EIT democratization within the Brazilian public health system (SUS) by providing a low-cost, portable solution for primary care in infrastructure-limited regions. At its current stage, TIME is a preclinical research prototype and is not intended for clinical use. Therefore, regulatory compliance was not assessed in this study. Clinical translation would require integration and validation of a real analog front-end, assessment of electrical safety and essential performance, risk management, and regulatory regularization according to the intended use and risk classification. Large-scale adoption in the SUS would additionally require clinical, economic, and implementation studies.

6 ETHICAL ASPECTS

This work uses exclusively public experimental data, collected and made openly available by FIPS. The datasets were originally produced by the KIT4 tomograph in physical phantoms, with no involvement of human beings, biological samples, or sensitive data [11]. All firmware development and validation scripts were carried out exclusively on these public data. For this reason, the work does not require submission to an Institutional Review Board / Research Ethics Committee, in accordance with CONEP guidelines.

Author contributions. Guilherme Corrêa Koller conducted the computational experiments and validation using the public FIPS datasets. Fábio Pires Itturriet supervised the study, with co-supervision by José Jair Alves Mendes Junior.

Acknowledgments. The authors thank the Universidade Tecnológica Federal do Paraná (UTFPR) for its institutional support.

Funding. This study received no specific funding.

Data and materials availability. The experimental datasets used in this study are publicly available from the FIPS data archive at https://doi.org/10.5281/zenodo.1203914. The project source code is available at https://github.com/guikoller/EIT.

Conflicts of interest. The authors declare no conflicts of interest.

Use of artificial intelligence. AI tools provided instrumental support in two stages: Google Gemini for manuscript writing, revision, and organization, and GitHub Copilot for source code implementation. The authors critically reviewed all generated content and take full responsibility for the manuscript's accuracy, interpretation, and scientific integrity.

REFERENCES

1. Mansouri S, Alharbi Y, Haddad F, Chabcoub S, Alshrouf A, Abd-Elghany AA. Electrical Impedance Tomography - Recent Applications and Developments. J Electr Bioimpedance. 2021;12(1):50-62. doi: https://doi.org/10.2478/joeb-2021-0007
2. Instituto Nacional de Câncer (Brasil). Controle do câncer de mama no Brasil: dados e números 2024 [Internet]. Rio de Janeiro: INCA; 2024 [cited 2026 Oct 31]. Available from: https://ninho.inca.gov.br/jspui/handle/123456789/17002
3. Adler A, Arnold JH, Bayford R, Borsic A, Brown B, Dixon P, et al. GREIT: a unified approach to 2D linear EIT reconstruction of lung images. Physiol Meas. 2009;30(6):S35-55. doi: https://doi.org/10.1088/0967-3334/30/6/S03
4. Barber DC, Brown BH. Applied potential tomography. J Phys E. 1984;17(9):723-33. doi: https://doi.org/10.1088/0022-3735/17/9/002
5. Rezanejad Gatabi Z, Mirhoseini M, Khajeali N, Rezanezhad Gatabi I, Dabbaghianamiri M, Dorri S. The Accuracy of Electrical Impedance Tomography for Breast Cancer Detection: A Systematic Review and Meta-Analysis. Breast J. 2022;2022:8565490. doi: https://doi.org/10.1155/2022/8565490
6. Zhu J, Snowden JC, Verdejo J, Chen E, Zhang P, Ghaednia H, et al. EIT-kit: An Electrical Impedance Tomography Toolkit for Health and Motion Sensing. In: UIST '21: The 34th Annual ACM Symposium on User Interface Software and Technology; 2021 Oct; Virtual Event, USA. New York (NY): ACM; 2021. p. 400-13. doi: https://doi.org/10.1145/3472749.3474758
7. San-Pablo-Juárez MÁ, Oropeza-Saucedo MM, Morales-Sánchez E. Computing of the Forward and Inverse Solutions of Electrical Impedance Tomography Using a 32-bit Microcontroller System. Comput Sist. 2025;29(2):995-1002. doi: https://doi.org/10.13053/cys-29-2-5696
8. Wang C, Lu W, Huang J, Guo Q, Zhou T, Zhao J, et al. Flexi-EIT: A Flexible and Reconfigurable Active Electrode Electrical Impedance Tomography System. IEEE Trans Biomed Circuits Syst. 2024;18(1):89-99. doi: https://doi.org/10.1109/TBCAS.2023.3307500
9. Lionheart WRB. EIT reconstruction algorithms: pitfalls, challenges and recent developments. Physiol Meas. 2004;25(1):125-42. doi: https://doi.org/10.1088/0967-3334/25/1/021
10. Pestana L, Miranda B. A Rapid Review on Advanced Software-in-the-Loop Methods for Automotive Software Verification. In: Anais do IX Simpósio Brasileiro de Testes de Software Sistemático e Automatizado (SAST 2024). Porto Alegre: Sociedade Brasileira de Computação; 2024. p. 56-65. doi: https://doi.org/10.5753/sast.2024.3883
11. Hauptmann A, Kolehmainen V, Mach NM, Savolainen T, Seppänen A, Siltanen S. Open 2D Electrical Impedance Tomography data archive. arXiv [Preprint]. 2017. doi: https://doi.org/10.48550/arXiv.1704.01178
12. Adler A, Lionheart WRB. Uses and abuses of EIDORS: an extensible software base for EIT. Physiol Meas. 2006;27(5):S25-42. doi: https://doi.org/10.1088/0967-3334/27/5/S03
13. STMicroelectronics. 32F769IDISCOVERY [Internet]. STMicroelectronics; 2024 [cited 2026 Apr 26]. Available from: https://www.st.com/en/evaluation-tools/32f769idiscovery.html

EDITORIAL NOTES

The Journal of Health Informatics is a scientific journal maintained by the Brazilian Society of Health Informatics (Sociedade Brasileira de Informática em Saúde), a non-profit scientific association dedicated to the development of Health Informatics and Digital Health in Brazil. The editorial process is conducted with scientific independence, free from institutional, commercial, or sponsor interference, and follows international best practices in publication ethics.

This article was double-blind peer reviewed by specialists in the field. The editorial team used artificial intelligence tools, under human supervision, in the initial screening, in checking the text, references and numbers and, when needed, in redrawing figures, charts and tables, which the authors approved in the proof. The tools and safeguards are described in the journal's Policy on the use of artificial intelligence. Editorial decisions were made by people.

SBIS Sociedade Brasileira de Informática em Saúde